atmosphere

MDPI

Article

The Impact of Scale-Aware Parameterization on the Next-Generation Global Prediction System in Taiwan for Front Predictions

Chang-Hung Lin [1,2,*], Ming-Jen Yang [1], Ling-Feng Hsiao [2] and Jen-Her Chen [2]

[1] Deportment of Atmospheric Sciences, National Taiwan University, No. 1 Sec. 4 Roosevelt Road, Taipei 10617, Taiwan; mingjen@as.ntu.edu.tw
[2] Central Weather Bureau, 64 Congyuan Road, Taipei 100006, Taiwan; lfh@cwb.gov.tw (L.-F.H.); river@cwb.gov.tw (J.-H.C.)
* Correspondence: changhong@cwb.gov.tw

Abstract: In order to improve the precipitation forecast of the next-generation Global Prediction System with the Finite-Volume Cubed-Sphere Dynamical Core in Taiwan's Central Weather Bureau, this study modified the convective processes in the New Simplified Arakawa-Schubert scheme based on the methodology of scale-aware parameterization developed in Kwon and Hong (2017) and investigated its impacts on a front event, which propagated across Taiwan and produced heavy rainfall in late May of 2020. Results show that the modified scale-aware parameterization has significantly improved the intensity and the spatial distribution of frontal precipitation forecasts due to the proper definition of convective updraft fraction. However, the synoptic-scale features perform a larger warm bias with the modified scale-aware parameterization. Therefore, further modification of the scale-aware capability of convective cloud water detrainment is proposed to reduce the heating from microphysical processes and result in a better overall performance for the medium-range weather forecasts.

Keywords: CWB FV3GFS; scale-aware parameterization; NSAS scheme; Mei-Yu front prediction

Citation: Lin, C.-H.; Yang, M.-J.; Hsiao, L.-F.; Chen, J.-H. The Impact of Scale-Aware Parameterization on the Next-Generation Global Prediction System in Taiwan for Front Predictions. *Atmosphere* **2022**, *13*, 1063. https://doi.org/10.3390/atmos13071063

Academic Editor: Eduardo García-Ortega

Received: 24 May 2022
Accepted: 1 July 2022
Published: 4 July 2022

1. Introduction

Several studies have suggested that moist convection plays an important role in adjusting the local and large-scale circulations [1–5]. Through its strong updrafts, deep convection vertically transports heat, water vapor, and momentum from the lower to the upper troposphere and influences the synoptic-scale distribution [5]. The condensation heating, precipitation, and compensating subsidence around the convective area produced by deep convection act to warm the troposphere and remove the moisture from the atmosphere. Both observation and numerical studies have demonstrated that the horizontal momentum transported upward by convection had a considerable effect on the zonal and meridional mean flow [6–9]. Moreover, the cloud radiative effect can influence the net radiative flux at the top of the atmosphere. For example, trapping longwave radiation can warm the troposphere, and reflecting shortwave solar radiation can cool the atmosphere. A reasonable representation of moist convection in numerical models is important to correctly predict atmospheric circulations. Since the temporal and spatial scales of cumulus convection are much smaller than the grid size of global forecast models or General Circulation Models, the subgrid-scale convective processes must be parameterized. However, due to the existence of uncertainty in convective parameterization, forecast errors may be largely produced by the convection scheme [10]. Therefore, numerous studies have attempted and have demonstrated that weather forecasts and climate simulations can be improved by revising the convective parameterization [11–14].

The National Oceanic and Atmospheric Administration (NOAA) has selected Finite-Volume Cubed-Sphere Dynamical Core (FV3), developed at the NOAA/Geophysical Fluid

Dynamics Laboratory (GFDL), as the dynamical core of the Next Generation Global Prediction System (NGGPS) to replace the Global Spectral Model (GSM) [15]. The physics package used in the NGGPS is largely the same as that in the National Centers for Environmental Prediction (NCEP) Global Forecast System (GFS), except that the Zhao–Carr microphysics parameterization [16] is replaced with the GFDL single-moment six-category cloud microphysics [17,18]. This new global model, which couples the FV3 dynamical core with the GFS physics package, is called FV3GFS [19]. Based on the FV3GFS, the Central Weather Bureau (CWB) of Taiwan has developed the next-generation operational global forecast model, named the CWB FV3GFS.

The New Simplified Arakawa-Schubert (NSAS) convection scheme [11] is used in CWB FV3GFS for operational weather forecasts. The simplified Arakawa–Schubert (SAS) scheme is based on the concepts proposed by Arakawa and Schubert (1974) [20] but is further modified and simplified by Grell (1993) [21] to consider saturated downdrafts and only one cloud type at a grid point, rather than the entire spectrum of cloud types. It employs a bulk mass flux approach that considers the exchange of mass between the environment and the vertical mass transport in convective plumes. The mass flux at the cloud base is determined from the assumption of convective quasi-equilibrium. The scheme is further modified by Han and Pan (2011) [12]. Various modifications include the increase in the maximum allowable cloud-base mass flux by defining a local Courant–Friedrichs–Lewy (CFL) criterion [22], the updated definition of entrainment and detrainment rates based on Bechtold et al. (2008) [23], considering the convective momentum transport, modified trigger condition and applied convective overshooting. Han et al. (2017) [11] have advanced the SAS scheme by adopting the scale-aware parameterization to suppress the contribution of the cumulus scheme as the horizontal resolution increases.

Through the investigation results of CWB FV3GFS with the NSAS scheme, some issues have been identified, especially in the vicinity of areas of Taiwan. For instance, too much light precipitation, less-organized convection, the underestimation of heavy rainfall frequency, and the weaker strength of mesoscale weather systems were found. Han et al. (2020) [24] have introduced the development of the convection scheme in the Korean Integrated Model (KIM), named KSAS scheme, which originated from the SAS convection scheme in the NCEP GFS [12]. Their study addressed problems in KIM that are related to the SAS convection scheme, including excessive light precipitation, less incoming solar radiation over the tropical oceans, the timing of the afternoon thunderstorm over land, and the wind bias in the tropical upper troposphere. To reduce these biases, the corresponding modifications include the revised trigger condition to be related to the relative humidity, enhanced entrainment rate by 10 times, revised autoconversion parameter to decrease the condensation with height, considering boundary layer forcing in the convective closures, revised convective momentum transport to have a less effective momentum mixing, and considering the scale-aware parameterization developed by Kwon and Hong 2017 (hereafter KH) [14].

On the other hand, Han et al., 2020 [24] proposed modifications to the cumulus parameterization scheme to improve the medium-range forecast skill for precipitation and large-scale fields. In addition, the modification of scale-awareness based on KH is an important improvement on the definition of the convective updraft fraction or by improving the scale dependency of the subgrid-scale cloud properties to increase the precipitation forecast skill and to capture the structures of convective systems, particularly over the tropics. Therefore, since the model biases, especially for the precipitation, and the version of the convection scheme in the CWB FV3GFS are similar to the KIM, the methodology described by KH is used to investigate its impacts on the prediction of major weather systems in the CWB FV3GFS.

During the late spring and early summer, a quasi-stationary front usually located over the east coast of China and extended to southern Japan is known as the Mei-Yu front. In this period, the organized mesoscale convective systems often develop along with the Mei-Yu system and result in significant precipitation over the East Asia region. In order

to improve the model's capability for Mei-Yu front predictions, we aim to evaluate the modified scale-aware parameterization based on KH and examine its impact on Mei-Yu front predictions in this study. Details of the model configuration and verification dataset are presented in Section 2. A comparison of scale-aware parameterization implemented in the NSAS and KSAS schemes is described in Section 3. The performance of the modified scale-aware parameterization on a Mei-Yu front forecast and the large-scale features are shown in Section 4. The summary and conclusions are given in Section 5.

2. Model Descriptions and Experimental Design

The CWB FV3GFS uses global cubed sphere C384 (~25 km grid spacing globally), and 64 vertical Semi-Lagrangian layers topped at 0.2 hPa. The physics package based on NCEP GFS physics, including the New Simplified Arakawa-Schubert shallow and deep convection schemes [12,20,21,25,26], which is further updated with scale-aware parameterization from Han et al. 2017 (hereafter NSAS) [11], GFDL microphysics scheme [17,18], orographic and convective gravity wave drag schemes [27–29], planetary boundary layer vertical diffusion scheme [30] and the Rapid Radiative Transfer Model scheme [31]. The numerical experiments in this study are integrated for 120 h with no data assimilation. The initial conditions are provided by the NCEP FV3GFS analysis data. For Mei-Yu front experiments, the forecasts are initialized at 0000 UTC each day from 14 May 2020 to 23 May 2020 (10 cases total). Furthermore, to statistically evaluate the performance of synoptic-scale features, the initialization time is extended from 23 May 2020 to 15 June 2020.

To investigate the influence of the modified scale-aware convection scheme on the CWB FV3GFS, this study examined the algorithm of scale-aware parameterization in the operational version of the NSAS scheme based on KH (Table 1; EXP experiment). A Mei-Yu front event that propagated across Taiwan during the period from 21 May to 23 May 2020 is selected to investigate the impact of scale-aware parameterization within the NSAS schemes. Moreover, in order to improve the forecasts, the modification of the detrained amount of convective cloud water is also examined in this study (EXPM experiment).

Table 1. Experiments and their descriptions.

EXP.	Description
CTRL	The operational version of the NSAS scheme in CWB FV3GFS.
EXP	The algorithm of scale-aware parameterization in the NSAS scheme is based on KH instead.
EXPM	As in the EXP experiment but the scale dependency of the amount of convective cloud water detrained into grid-scale condensate is ignored.

The verifications of geopotential height, temperature, specific humidity, horizontal and vertical velocities, and relative vorticity from all experiments in this paper are evaluated against the European Centre for Medium-Range Weather Forecasts (ECMWF) new reanalysis product (ECMWF Reanalysis v5; ERA5). The dataset has approximately 30-km horizontal resolution and 137 vertical levels, with the model top at the height of 80 km and the temporal resolution of 1 h. The Integrated Multi-Satellite Retrievals for Global Precipitation Measurement (IMERG) product is used to verify the precipitation forecast score over Asia (5° S~55° N, 60° E~180° E). The horizontal resolution of the Global Precipitation Measurement (GPM) dataset is about 0.1° × 0.1° with a temporal resolution of 1 h.

3. Scale-Aware Parameterization in NSAS Scheme

The traditional convection parameterization schemes were designed under the assumption that the fractional areas of convective updraft only cover less than about 10% of the model grid box area. However, since the increasing computer power is available to reduce the model grid spacing and the convective updrafts are not negligibly small, the subgrid-scale processes become partially resolved. Hence, the previous assumption

for convection schemes is not valid anymore. To alleviate the issues when using the traditional convection schemes, the scale-aware parameterization based on Arakawa and Wu (2013) [25] is considered in the operational version of the NSAS scheme in the CWB FV3GFS where the convective updraft mass flux is decreasing with increasing fractional cloud coverage. In the operational version of the scale-aware NSAS scheme, the cloud-base mass flux (M_u) is defined as

$$M_u = (1 - \sigma_u)^2 M_u^{org}, \tag{1}$$

where σ_u is the fractional cloud coverage, a subscript u denotes an updraft, and a superscript org represents an original value. Based on Grell and Freitas (2014) [26], the σ_u is determined as

$$\begin{gathered} \sigma_u = \frac{3.14R_c^2}{A_{grid}} \; and \\ R_c = \frac{0.2}{\varepsilon_0} \end{gathered} \tag{2}$$

where R_c is the radius of the convective updraft, A_{grid} is the model grid box area, ε_0 is the entrainment rate at cloud base height. The definition of R_c in Equation (2) is assumed that the radius of convective updraft is given to be inversely proportional to the entrainment rate since the entrainment effect plays a role in suppressing the development of convection. The parameter σ_u approaches zero when the grid box area is much larger than the convection area, and the scale-aware convection scheme restores the traditional convection scheme. As the model horizontal resolution is increased and the convective physical processes can be partially resolved, σ_u is set to close to one, and the cumulus activity is gradually reduced.

From the definition of σ_u, the successful development of a scale-ware convection scheme is related to the proper definition of convective updraft fraction. Following the concept based on Arakawa and Wu (2013) [25], KH separated σ_u into two quantities of scale-aware coefficients (σ_1 and σ_2). In addition, the cloud-base mass flux, convective trigger function (TRG), and convective cloud water detrainment (DTR) are assumed to be scale-aware capabilities as follows

$$\begin{gathered} M_u = (1 - \sigma_1)(1 - \sigma_2) M_u^{org}, \\ TRG = (1 - \sigma_1) TRG^{org}, \\ DTR = \sigma_1 DTR^{org} \end{gathered} \tag{3}$$

where σ_1 is a function of horizontal grid size (Δx) as in Equation (4):

$$\begin{gathered} \sigma_1 = 1 - \frac{1}{\pi}\left\{\sigma_{con}\left[(\Delta x - 5000) + \frac{\pi}{2}\right]\right\} \; and \\ \sigma_{con} = tan(0.4\pi) \; / (5000 - 1000) \end{gathered} \tag{4}$$

The constant values of 5000 and 1000 are set to determine the shape of the curve for σ_1. As the horizontal resolution increase, the value of σ_1 approaches to one. Therefore, both the vertical eddy transport and the trigger for deep convection are suppressed, and the subgrid-scale cloud water detrained into grid-scale condensate is increased.

The other scale-aware coefficient σ_2 is defined as

$$\sigma_2 = \frac{\overline{w}}{\overline{w}_c} \tag{5}$$

where $\overline{w}$ and $\overline{w}_c$ are the grid scale and subgrid-scale vertical velocities, respectively. The overbar denotes the vertical average between cloud base and top. The definition of σ_2 considers that the area of convective updraft is influenced by the thermodynamic and dynamical conditions of the atmosphere. As the strength of the grid-scale vertical velocity approaches the subgrid-scale updraft, the development of convective updraft becomes dominant in the model grid box [32], and the amount of σ_2 is increased to suppress the role of the convection scheme.

4. Results

4.1. Mei-Yu Precipitation

Figure 1 presents the 48–72 h precipitation forecast results and the GPM-IMERG rainfall data during the period from 21 May to 23 May 2020. From the observation (Figure 1a–c), the Mei-Yu front presents a west-south to east-north (southwest-northeast oriented) alignment and moves across Taiwan from the north. Additionally, an intensive mesoscale convective system (MCS) was developed at the southern part of the front on 22 May 2020. In the CTRL experiment (Figure 1d–f), the results show that the intensity and the structure of the predicted frontal precipitation are underestimated and less organized (compared to the GPM observations). Moreover, the front is still located over northern Taiwan on 22 May; in other words, the predicted propagation speed of the front is slower than the observation. In the EXP experiment (Figure 1g–i), the intensity of Mei-Yu front precipitation is significantly increased, especially for the MCS developed at the southern part of the front. The main features of the Mei-Yu front evolution are well captured by the EXP experiment than that of CTRL.

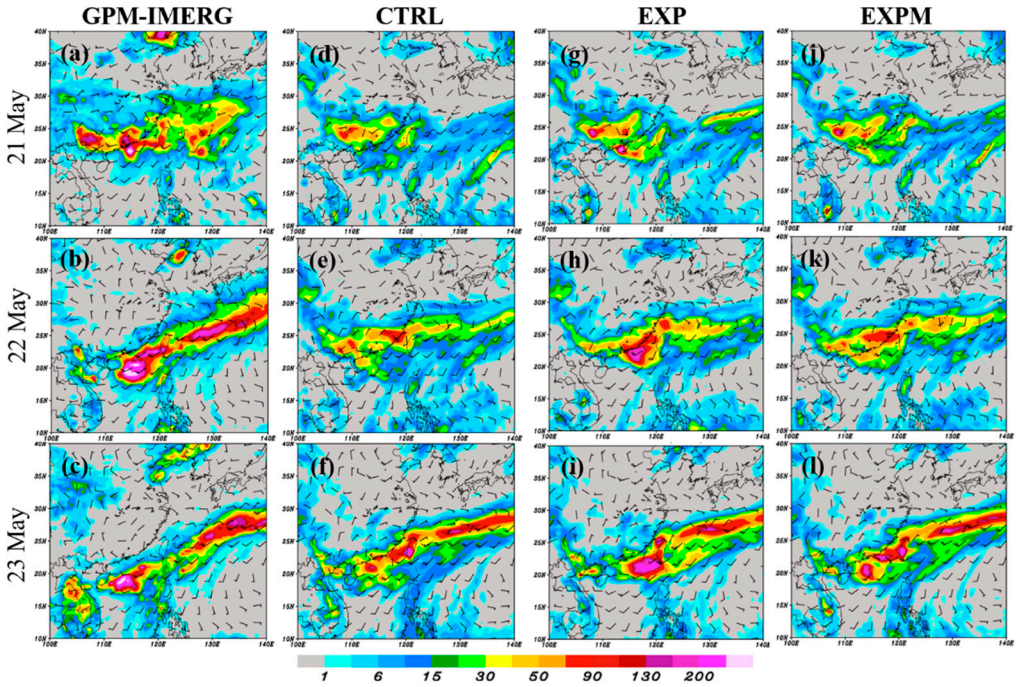

Figure 1. Daily precipitation (mm; shaded) in (**a**) 21 May, (**b**) 22 May, (**c**) 23 May 2020 from GPM-IMERG rainfall data. The 48–72 h accumulated rainfall from the forecast validated in (**d**) 21 May, (**e**) 22 May, (**f**) 23 May for the CTRL experiment. (**g**–**i**) and (**j**–**l**) as in panels (**d**–**f**), except for EXP and EXPM experiments, respectively.

To illustrate the precipitation forecast skill for the modified scheme over Asia (5° S ~55° N, 60° E~180° E), four skill scores including threat score (TS), bias score (BIAS), probability of detection (POD) and false alarm ratio (FAR) are evaluated with different precipitation thresholds (Figure 2). Although the results show that the forecast skill scores were very similar in TS, POD, and FAR between the EXP and CTRL experiments, the BIAS scores have been significantly reduced with the EXP experiment. It indicated that the over-forecasting of light precipitation (less than 5 mm day^{-1}) and under-forecasting of heavy precipitation (larger than 20 mm day^{-1}) were improved compared to that of the CTRL experiment. In other words, the modification of the scale-aware parameterization in the NSAS scheme based on KH had a better result in predicting the frontal precipitation in the vicinity of Taiwan, which is consistent with the horizontal distribution of precipitation shown in Figure 1.

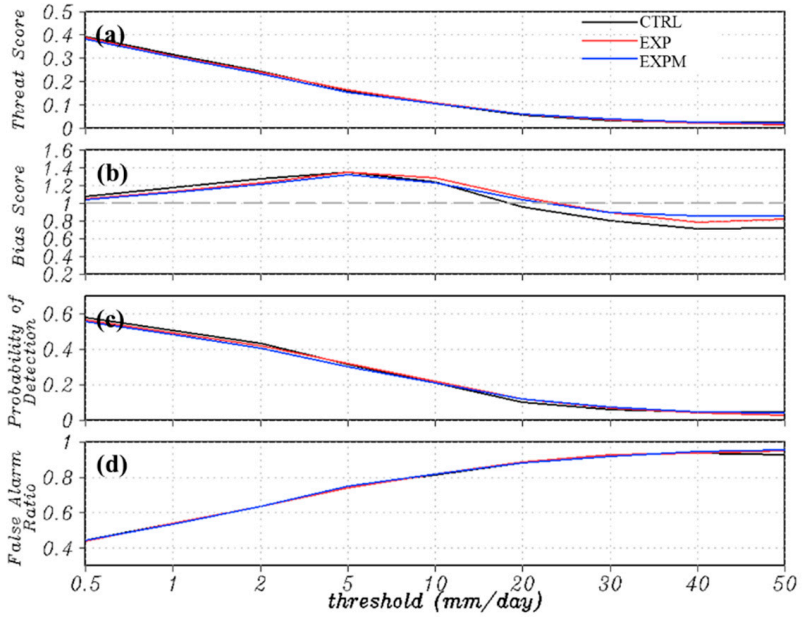

Figure 2. (**a**) Threat score, (**b**) bias score, (**c**) probability of detection, and (**d**) false alarm ratio of precipitation averaged over Asia (5° S~55° N, 60° E~180° E) from 14 May to 23 May 2020 for 48–72 h accumulated rainfall with different thresholds from the CTRL (black line), EXP (red line) and EXPM (blue line) experiments.

On the other hand, the vertical cross-sections of horizontal moisture advection and relative vorticity perpendicular to the front within ±5° are further illustrated in Figure 3, which shows the impacts of modified convection schemes on the vertical structure of the Mei-Yu front. The frontal positions were determined by the maximum vorticity axes at 850 hPa. Due to more intense horizontal moisture advection associated with stronger southerly flow in the lower troposphere for the EXP experiment (Figure 3c), the result shows a stronger moisture convergence and vorticity at the front center than that of the CTRL experiment (Figure 3b). Furthermore, the vertical structure of vorticity in EXP was tilted slightly northward with height, which is more similar to the ERA5 reanalysis (Figure 3a), although the intensity of the frontal system was generally weaker than in the ERA5 reanalysis.

Further investigation of the variation of convective trigger effect with different experiments is shown in Figure 4. It indicates the contribution of the cumulus scheme (subgrid-scale precipitation) and microphysics scheme (grid-scale precipitation) to the total precipitation. The frontal precipitation was mainly dominated by the grid-scale precipitation due to the grid cell-averaged relative humidity saturation, while the subgrid-scale precipitation was located at the leading edge of the frontal system (Figure 4a,b). A similar result was obtained by the EXP experiment (Figure 4c,d). However, the EXP produced larger convective precipitation at the leading age of the front, which reveals that more intense convection had been triggered. As a result, the microphysics scheme contributes to a more widespread and enormous grid-scale precipitation at the center of the Mei-Yu frontal system due to stronger horizontal moisture convergence. The results are in agreement with Figure 3.

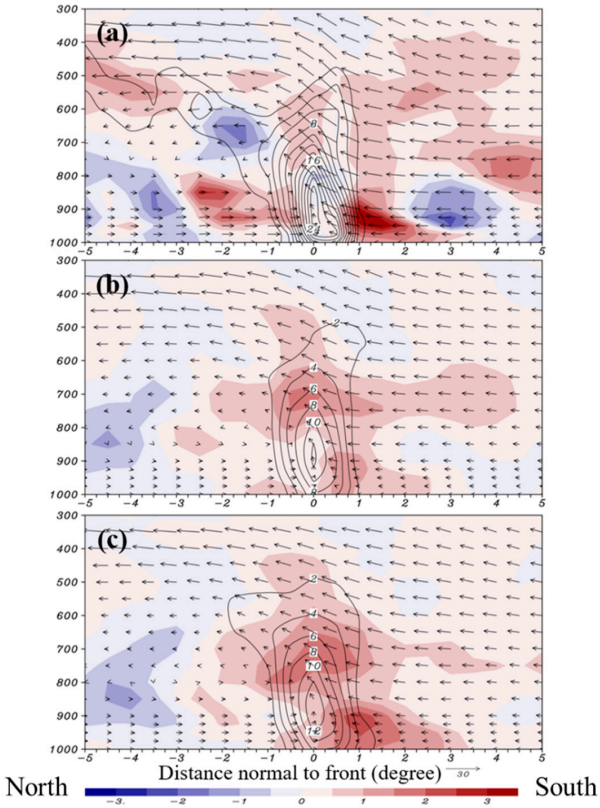

Figure 3. Vertical cross-sections averaged during the mature stage (from 0000 UTC 22 May to 0000 UTC 23 May 2020) of Mei-Yu front from (**a**) ERA5 reanalysis data and from the different initial date (from 0000 UTC 17 May to 0000 UTC 22 May 2020) in the (**b**) CTRL and (**c**) EXP experiments. Colored is the horizontal moisture advection (g kg^{-1} 6 h^{-1}). Contours are the relative vorticity (10^5 s^{-1}). Vectors are the vertical circulation perpendicular to the front (30 m s^{-1}). The frontal positions are determined by the maximum vorticity axes at 850-hPa. The cross-section is perpendicular to the front within ±5° (positive toward the south) and is averaged along the frontal length.

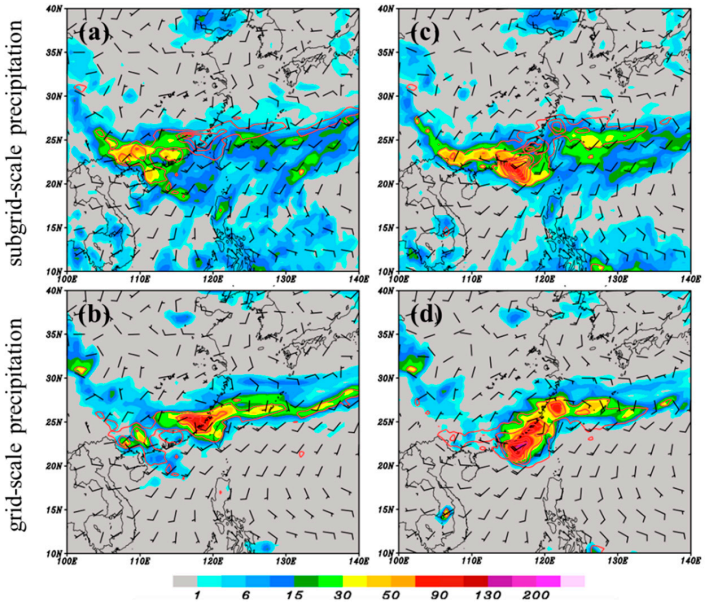

Figure 4. (**a**) Subgrid-scale and (**b**) grid-scale precipitation (colored; mm) for 48–72 h accumulated from the CTRL experiment on 21 May 2020. Red contours are the total precipitation (combination of subgrid-scale and grid-scale precipitation). (**c**,**d**) as in (**a**,**b**) but for the EXP experiment.

4.2. Large-Scale Verifications

The accuracy of large-scale circulation forecast can significantly influence the quality of local weather prediction through the variations of environment for synoptic-scale and convective-scale processes [19]. Therefore, the assessment of synoptic-scale prediction is essential for the GFS. To gain further insight into the impact of the scale-aware parameterization in the NSAS convection scheme on the prediction of Mei-Yu event, we also examined the performance of synoptic-scale features for these two experiments. Hence, the large-scale fields of the medium-range forecasts over Asia (5° S~55° N, 60° E~180° E) were statistically evaluated during the daily forecasts started from 0000 UTC 15 May 2020 to 0000 UTC 15 June 2020 (32 cases total). Figure 5 presents the vertical profiles of biases for 96~120 h forecast against ERA5 reanalysis data. The results from the EXP experiment show an improved forecast skill of specific humidity in the whole atmosphere. However, the temperature and geopotential height presented larger warm and negative biases in the low-to-mid levels of the troposphere, respectively. To understand the reason for the warm bias in EXP, we investigated the horizontal distributions of 900 hPa temperature bias, precipitation, surface heat fluxes, and apparent moisture sink to attempt to reduce the biases for the EXP experiment.

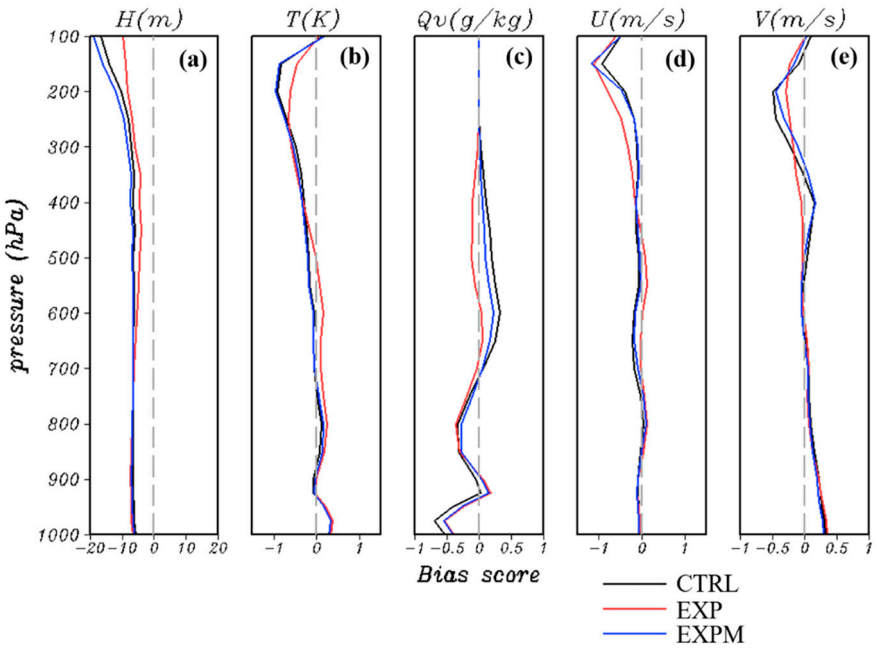

Figure 5. Vertical profiles of the biases of (**a**) geopotential height (m), (**b**) temperature (K), (**c**) specific humidity (g/kg), (**d**) zonal and (**e**) meridional wind (m/s) averaged over Asia (5° S~55° N, 60° E~180° E) for 96~120 h forecast based on 32 daily cases from 0000 UTC 15 May 2020 to 0000 UTC 15 June 2020 against ERA5 reanalysis data from CTRL (black line), EXP (red line), and EXPM (blue line) experiments.

The averaged horizontal distributions of 900 hPa temperature bias over Asia for 96~120 h against ERA5 reanalysis data are shown in Figure 6. Both CTRL (Figure 6a) and EXP (Figure 6b) experiments show that the occurrence of warm bias was mainly located in the land areas, and the cold bias mainly occurred over the oceanic regions. The larger warm bias in EXP mainly appeared over Mainland Southeast Asia, Borneo, and the archipelagos of Indonesia (Figure 7b). Meanwhile, a negative bias of 900 hPa geopotential height presented significantly over these areas (Figure 7a) compared to the ERA5 data and CTRL experiment. Therefore, the possible reasons for the occurrence of a larger warm bias in EXP may be excessive surface heating due to the surface heat flux or the overestimated latent heat flux due to the development of convection. In order to verify the speculations, the surface heat flux and apparent moisture sink were investigated.

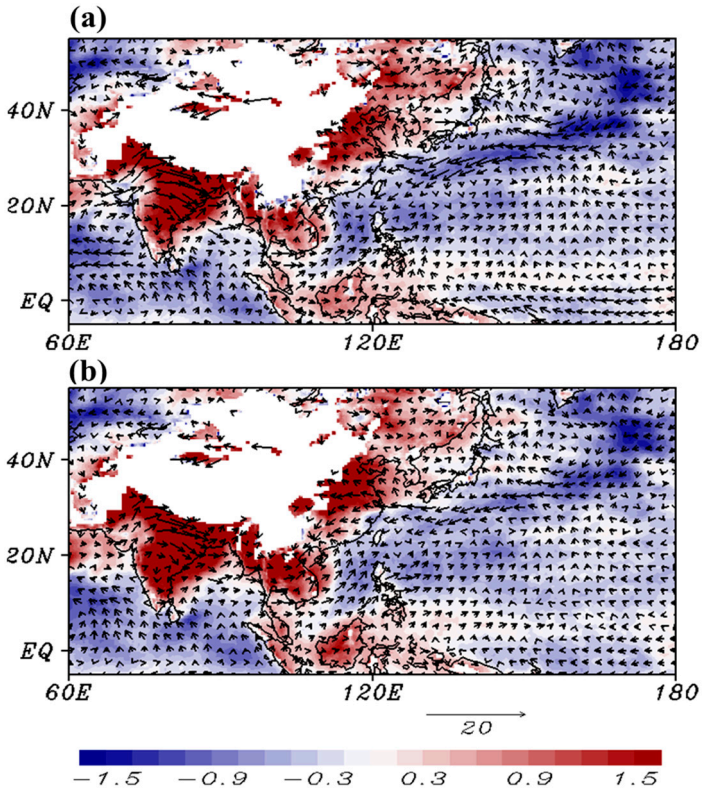

Figure 6. Biases of 900 hPa temperature (K) averaged over 96~120 h forecast based on 32 daily cases from 0000 UTC 15 May 2020 to 0000 UTC 15 June 2020 from (**a**) CTRL and (**b**) EXP experiments.

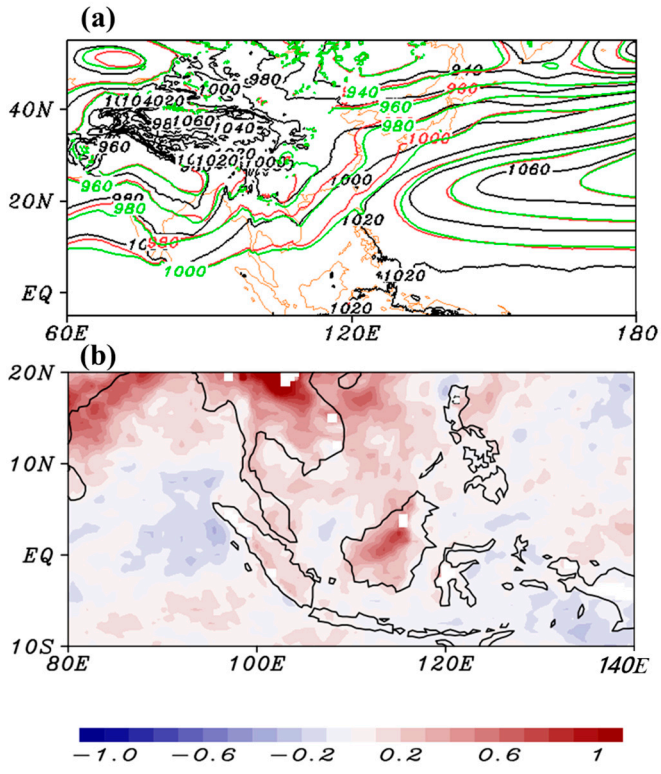

Figure 7. (**a**) 900-hPa geopotential height (m) averaged over 96~120 h forecast based on 32 daily cases from 0000 UTC 15 May 2020 to 0000 UTC 15 June 2020 from the CTRL (red contour) and EXP (green contour) experiments. The Black contour in (**a**) is the result obtained from ERA5 reanalysis data. (**b**) the difference in temperature (K) for 96~120 h forecast between EXP and CTRL experiments.

The difference in surface heat fluxes between EXP and CTRL is shown in Figure 8. EXP generally increased the incoming shortwave radiation over the maritime continent (Figure 8a) and the upward sensible heat flux on the land areas, indicating that the EXP experiment reduced the cloud cover over East Asia. Besides, since the updated scale-aware parameterization tended to produce stronger convection and precipitation when the large-scale convergence was present, the upward surface latent heat flux was increased on the windward side of the terrain. Clearly, these findings indicate that the increase in upward sensible and latent heat fluxes in the EXP experiment caused excessive warming in the lower atmosphere.

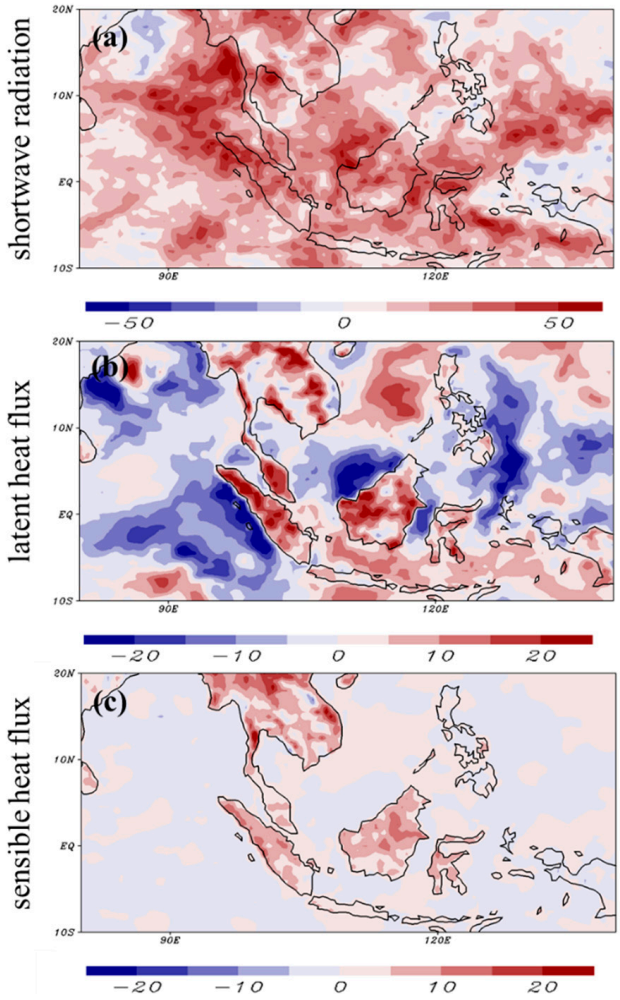

Figure 8. Differences in (**a**) shortwave radiation (w m^{-2}; a positive value indicates downward), (**b**) latent heat flux (w m^{-2}; a positive value indicates upward) and (**c**) sensible heat flux (w m^{-2}; a positive value indicates upward) between EXP and CTRL experiments averaged over 96~120 h forecast based on 32 daily cases from 0000 UTC 15 May 2020 to 0000 UTC 15 June 2020.

According to Yanai et al. (1973), the apparent moisture sink (Q_2; Ks^{-1}) represents the latent heating due to the net condensation and subgrid-scale moisture flux convergence

$$\begin{aligned} Q_2 &= -L\left(\frac{\partial q}{\partial t} + \nabla \cdot qV + \frac{\partial q\omega}{\partial p}\right) \\ &= L(c-e) + L\frac{\partial q'\omega'}{\partial p} \end{aligned} \quad (6)$$

where q is the specific humidity (gkg^{-1}); V is the horizontal wind (ms^{-1}); ω is the vertical wind speed (Pa s^{-1}); L is the latent heat coefficient of evaporation (Jkg^{-1}). To investigate

the averaged heating profile due to the development of convection in the CTRL and EXP experiments, the vertical integrated Q_2 from 1000 to 700 hPa was investigated.

Comparing the difference of vertical integrated Q_2 (mm day^{-1}) computed against ERA5 reanalysis data for 96~120 h forecast from CTRL and EXP experiments (Figure 9), it was found that both the CTRL and EXP experiments generally overestimated the strength of convection developing over the terrain areas, resulting in a positive bias of latent heating due to the overestimated condensation process. In EXP, the bias of latent heating was larger than that in the CTRL, especially on the windward side of the terrain. The result indicates that the EXP experiment tends to produce more active convection due to the terrain effect, leading to an overestimated latent heat release when water condenses.

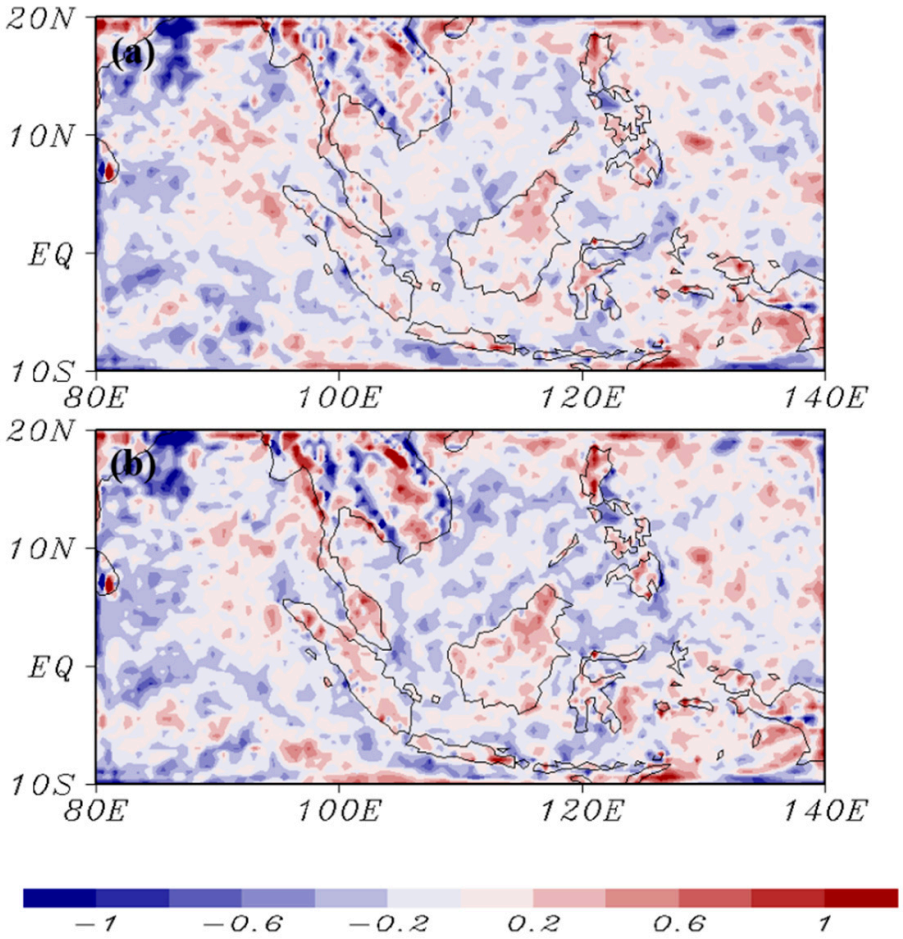

Figure 9. Difference of vertical integrated apparent moisture sink (Q_2; mm/day) from 1000 hPa to 700 hPa for 96~120 h forecast based on 32 daily cases from 0000 UTC 15 May 2020 to 0000 UTC 15 June 2020 computed against ERA5 reanalysis data from (**a**) CTRL and (**b**) EXP experiments.

According to the investigation results from surface heat fluxes and Q_2, the EXP overestimates the development of convection over Southeast Asia, especially on the windward side of the terrain, leading to larger latent heating caused by the precipitation process that water vapor condenses into rainwater. As with the increase in precipitation, the decrease in cloud cover leads to an enhancement of incoming solar radiation. Consequently, through the sensible and latent heating processes, the overprediction of warming appeared in the lower troposphere.

4.3. Further Modification of NSAS Scheme

To further understand the temperature tendencies from different physical processes in the CTRL and EXP experiments, the heating rate (K/6-h) due to each physical parameterization, including boundary layer, gravity wave drag, deep convection, shallow convection, microphysics, and radiation schemes, were investigated. The profiles of temperature tendencies from the CTRL experiment (Figure 10a) averaged over Asia (5° S~55° N, 60° E~180° E) for 96~120 h forecast revealed strong heating from the deep convection scheme in the entire troposphere due to the subgrid-scale condensation heating. The maximum value was located at 500 hPa. In the lower troposphere, the shallow and planetary boundary layer schemes were the main contributors to the heating rate. The radiation and microphysics schemes presented a cooling rate in the entire troposphere, which were produced by radiative cooling and grid-scale evaporation and melting processes, respectively. The contribution from the gravity wave drag scheme was minor compared to the other physical processes. The difference in heating/cooling rate between the EXP and CTRL experiments is shown in Figure 10b. It appears that the updated scale-ware parameterization enormously reduced the deep convection heating and enhanced the microphysical heating in the mid-level troposphere, while the shallow convection heating is slightly increased below approximately 600 hPa. Changes in temperature by the other physical processes were negligible. Hence, the occurrence of a larger warm bias in low-to-mid levels from the EXP is attributed to the decrease in subgrid-scale water vapor consumption by the deep convection process and the increase in grid-scale condensation heating resulting from the consumption of environmental instability by microphysical processes. According to the descriptions in Han et al. (2020) [24], while the scale dependency of the amount of convective cloud water detrained into grid-scale condensate is considered, the condensation heating will be enhanced by the microphysical processes (see Figure 7 of Han et al. 2020) [24]. Therefore, to remedy the unrealistic heating profile resulting in a larger warm bias mentioned above, we ignored the scale-aware capability of convective cloud water detrainment in the EXP experiment (EXPM experiment; Table 1). In other words, the scale-aware coefficient σ_1 was removed when the convection scheme is calculating the convective cloud water detrainment (Equation (3); DTR). Figure 10c presents that the EXPM experiment substantially reduced the heating by microphysical processes and decreased the warm bias in the low-to-mid levels from the EXP experiment (Figure 5), leading to the biases of temperature, geopotential height, and horizontal wind compared to the CTRL experiment. The effects of the modification in our study are consistent with the results described in Han et al. (2020) [24]. Moreover, the EXPM experiment still can alleviate the dry bias below 700 hPa in the CTRL experiment. The horizontal distribution of frontal precipitation showed that the EXPM experiment (Figure 1j–l) significantly enhanced the strength of the precipitation rate, especially in the eastern part of the front, leading to a more organized linear convective system compared to the CTRL experiment (Figure 1d–f). Although the strength of the MCS developed at the southern part of the front is less than that in the EXP experiment (Figure 1g–i), the intensity and the development of MCS in CTRL were improved by the EXPM experiment. From the evaluation of precipitation forecast skill scores (Figure 2), the EXPM appears to have a similar result to the EXP; that is, the EXPM experiment still could reduce the systematic bias in the frontal precipitation. In summary, the EXPM experiment not only improved the simulations of frontal precipitation and the water vapor in the lower troposphere during the period from 15 May 2020 to 15 June 2020 but also maintained the forecast skill of the synoptic-scale weather systems.

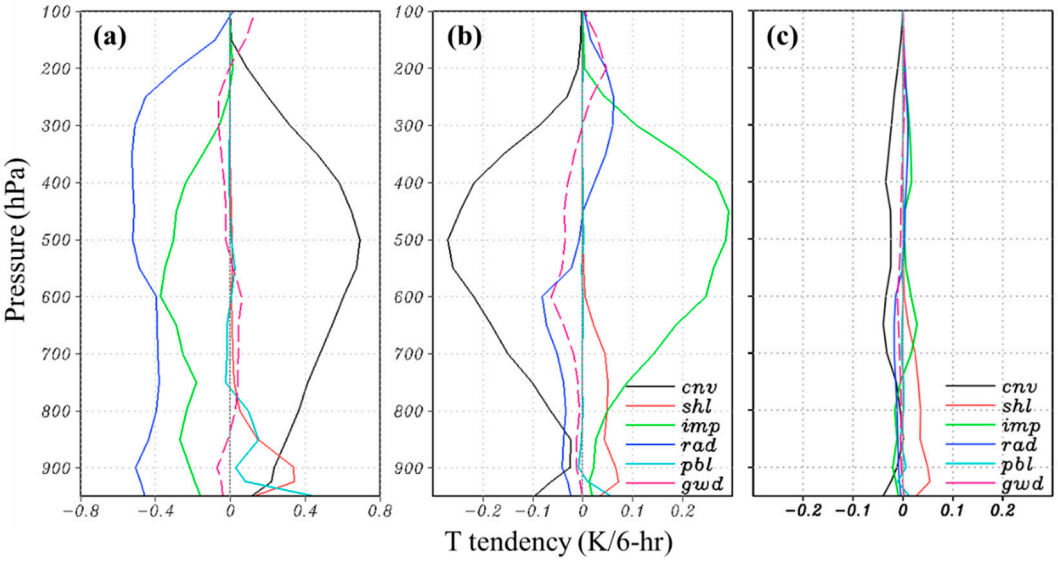

Figure 10. Vertical profile of temperature tendencies (K/6 h) due to the different physical processes in CWB FV3GFS averaged over Asia (−5° N~55° N, 60° E~180° E) for 96~120 h forecast based on 32 daily cases from 0000 UTC 15 May 2020 to 0000 UTC 15 June 2020 from (**a**) CTRL experiment and the effects of (**b**) EXP and (**c**) EXPM experiments.

5. Summary and Conclusions

The examinations of replacing the scale-aware parameterization in the NSAS scheme from the operational version [11] in the CWB FV3GFS to the KSAS version developed by KH have been conducted in this study. The operational version of the NSAS deep convection scheme is based on Arakawa and Schubert (1974) [20], which used a quasi-equilibrium assumption as a closure, and was simplified by Grell (1993) [21] to employ a bulk mass-flux approach and consider a single cloud type at each grid point. Han et al. (2017) [11] proposed a scale-aware parameterization for the convection scheme, which assumes that the convective updraft mass flux decreases with the increasing area of cloud coverage to improve the medium-range forecast as the model grid size increases. The cloud coverage is assumed to be inversely proportional to the entrainment rate [26]. However, the proper definition of convective updraft fraction is an important component in the development of scale awareness for convection schemes. KH has developed another method that the scale-aware coefficient is related to a ratio of grid point vertical velocity over the convective updraft velocity and has assumed that the physical processes of updraft mass flux, trigger condition, and the cloud water detrained into grid-scale condensate are all scale-ware capabilities.

A Mei-Yu front event from 21 May 2020 to 23 May 2020 has been selected to investigate the impact and the performance of the modified scale-aware parameterization on the CWB FV3GFS. According to the investigation results of frontal precipitation and the vertical structure (compared to the CTRL experiment), because the EXP experiment has decreased the occurrence of convection over the downstream areas (east side) of the frontal system, more intensive moisture advection appeared at the leading edge of the front leads to a more active vertical motion and precipitation at the center of the frontal system. Therefore, the EXP experiment has significantly reduced the systematic biases of excessive light precipitation and underestimated heavy rainfall. Although the mesoscale features are well captured in the EXP experiment, the forecast skill for large-scale fields appears that the EXP experiment tends to produce larger warm temperature and negative geopotential height biases than those in the CTRL experiment, especially over Mainland Southeast Asia. From a series of verifications, it shows that the EXP experiment overestimates the latent heating associated with the condensation of cloud water in the low-to-mid troposphere, resulting in excessive surface precipitation, less cloud cover, and an increase in incoming

shortwave radiation. Hence, larger heating emerges in the lower troposphere due to the overestimated surface sensible heat and latent heat fluxes. To alleviate the systematic biases in the large-scale forecast, the EXP experiment has been further modified.

The result of the temperature tendencies from each physical parameterization appears that the contribution of larger warming in the low-to-mid troposphere from the EXP experiment is dominated by microphysical heating since the consumption of convective cloud water by deep convection process is decreased. Therefore, we have further modified the EXP experiment so that the scale dependency of convective cloud water detrainment is ignored (EXPM experiment) to decrease the condensation heating. The EXPM experiment has successfully reduced the biases of warm temperature and the other large-scale fields to be comparable to the CTRL experiment and has presented a better forecast skill for the frontal precipitation than that in the CTRL experiment.

Through the experiments of replacing the scale-aware parameterization, we understand the impact of each modified physical process and the interaction between convective and microphysical parameterization schemes. Although results in this study show that the EXPM experiment can improve the performance of a Mei-Yu front event, more cases are needed to have statistically meaningful conclusions. In addition, the corresponding mechanisms that lead to increased heating from the shallow convection scheme in the EXPM and EXP experiments (Figure 10b,c) still remain unknown, which need to be further addressed in the future.

Author Contributions: C.-H.L. conducted the real-time results, plotted the figures, and wrote the original manuscript. M.-J.Y., L.-F.H. and J.-H.C. discussed the results and reviewed and edited the manuscript. All authors have read and agreed to the published version of the manuscript.

Funding: This research received no external funding.

Institutional Review Board Statement: Not applicable.

Informed Consent Statement: Not applicable.

Data Availability Statement: The data presented in this study are available upon request from the corresponding author. The data are not publicly available due to embargo under project data policy through December 2022.

Acknowledgments: This study is carried out through a project funded by the Central Weather Bureau (CWB) in Taiwan. We are extremely grateful for the computational resources and the assistance provided by the CWB. The ERA5 reanalysis data can be obtained from the Computational and Information Systems Laboratory at the National Center for Atmospheric Research archived at https://rda.ucar.edu/datasets/ds633.0/ (accessed on 1 December 2021) [33]. The GPM (IMGERG v06) data used in this study is obtained from the NASA Goddard Earth Sciences (GES) Data and Information Services Center (DISC) [34]. We appreciate the helpful comments from anonymous reviewers that improved the manuscript.

Conflicts of Interest: The authors declare no conflict of interest.

Abbreviations

The following abbreviations are used in this manuscript:

BIAS	Bias Score
CFL	Courant–Friedrichs–Lewy
DISC	Data and Information Services Center
DTR	Convective Cloud Water Detrainment
ECMWF	European Centre for Medium-Range Weather Forecasts
FAR	False Alarm Ratio
FV3	Finite-Volume Cubed-Sphere Dynamical Core
GES	Goddard Earth Sciences
GFDL	Geophysical Fluid Dynamics Laboratory

GFS	Global Forecast System
GPM	Global Precipitation Measurement
GSM	Global Spectral Model
IMERG	Integrated Multi-Satellite Retrievals for Global Precipitation Measurement
KH	Kwon and Hong 2017
KIM	Korean Integrated Model
MCS	Mesoscale Convective System
NOAA	National Oceanic and Atmospheric Administration
NGGPS	Next Generation Global Prediction System
NCEP	National Centers for Environmental Prediction
NSAS	New Simplified Arakawa-Schubert
POD	Probability of Detection
SAS	Simplified Arakawa–Schubert
TRG	Convective Trigger Function
TS	Threat Score

References

1. Randall, D.A.; Abeles, J.A.; Corsetti, T.G. Seasonal simulations of the planetary boundary layer and boundary-layer stratocumulus clouds with a general circulation model. *J. Atmos. Sci.* **1985**, *42*, 641–675. [CrossRef]
2. Steinheimer, M.; Hantel, M.; Bechtold, P. Convection in Lorenz's global energy cycle with the ECMWF model. *Tellus* **2008**, *60*, 1001–1022. [CrossRef]
3. Stensrud, D.J. Effects of a persistent, midlatitude mesoscale region of convection on the large-scale environment during the warm season. *J. Atmos. Sci.* **1996**, *53*, 3503–3527. [CrossRef]
4. Stensrud, D.J.; Anderson, J.L. Is midlatitude convection an active or a passive player in producing global circulation patterns? *J. Clim.* **2001**, *14*, 2222–2237. [CrossRef]
5. Tiedtke, M. Parameterization of cumulus convection in large-scale models. In *Physically-Based Modelling and Simulation of Climate and Climatic Change*; Schlesinger, M.E., Ed.; D. Reidel: Gothenburg, Sweden, 1988; pp. 375–431.
6. LeMone, M.A. Momentum Transport by a Line of Cumulonimbus. *J. Atmos. Sci.* **1983**, *40*, 1815–1834. [CrossRef]
7. Moncrieff, M.W.; Liu, C. Representing Convective Organization in Prediction Models by a Hybrid Strategy. *J. Atmos. Sci.* **2006**, *63*, 3404–3420. [CrossRef]
8. Badlan, R.L.; Lane, T.P.; Moncrieff, M.W.; Jakob, C. Insights into convective momentum transport and its parametrization from idealized simulations of organized convection. *Quart. J. Roy. Meteor. Soc.* **2017**, *143*, 2687–2702. [CrossRef]
9. Liu, Y.-C.; Fan, J.; Xu, K.-M.; Zhang, G.J. Analysis of Cloud-Resolving Model Simulations for Scale Dependence of Convective Momentum Transport. *J. Atmos. Sci.* **2018**, *75*, 2445–2472. [CrossRef]
10. Tiedtke, M. A comprehensive mass flux scheme for cumulus parameterization in large-scale models. *Mon. Weather Rev.* **1989**, *117*, 1779–1800. [CrossRef]
11. Han, J.; Wang, W.; Kwon, Y.C.; Hong, S.-Y.; Tallapragada, V.; Yang, F. Updates in the NCEP GFS Cumulus Convection Schemes with Scale and Aerosol Awareness. *Weather Forecast.* **2017**, *32*, 2005–2017. [CrossRef]
12. Han, J.; Pan, H.-L. Revision of convection and vertical diffusion schemes in the NCEP global forecast system. *Weather Forecast.* **2011**, *26*, 520–533. [CrossRef]
13. Bechtold, P.; Semane, N.; Lopez, P.; Chaboureau, J.-P.; Beljaars, A.; Bormann, N. Representing equilibrium and nonequilibrium convection in large-scale models. *J. Atmos. Sci.* **2014**, *71*, 734–753. [CrossRef]
14. Kwon, Y.C.; Hong, S.-Y. A Mass-Flux Cumulus Parameterization Scheme across Gray-Zone Resolutions. *Mon. Weather Rev.* **2017**, *145*, 583–598. [CrossRef]
15. Sela, J.G. Spectral modeling at the National Meteorological Center. *Mon. Weather Rev.* **1980**, *108*, 1279–1292. [CrossRef]
16. Zhao, Q.Y.; Carr, F.H. A prognostic cloud scheme for operational NWP models. *Mon. Weather Rev.* **1997**, *125*, 1931–1953. [CrossRef]
17. Chen, J.H.; Lin, S.J. The remarkable predictability of inter-annual variability of Atlantic hurricanes during the past decade. *Geophys. Res. Lett.* **2011**, *38*, L11804. [CrossRef]
18. Chen, J.H.; Lin, S.J. Seasonal predictions of tropical cyclones using a 25-km-resolution general circulation model. *J. Clim.* **2013**, *26*, 380–398. [CrossRef]
19. Zhou, L.; Lin, S.-J.; Chen, J.-H.; Harris, L.M.; Chen, X.; Rees, S. Toward convective-scale prediction within the Next Generation Global Prediction System. *Bull. Amer. Meteor. Soc.* **2019**, *100*, 1225–1243. [CrossRef]
20. Arakawa, A.; Schubert, W.H. Interaction of a Cumulus Cloud Ensemble with the Large-Scale Environment, Part I. *J. Atmos. Sci.* **1974**, *31*, 674–701. [CrossRef]
21. Grell, G.A. Prognostic evaluation of assumptions used by cumulus parameterizations. *Mon. Weather Rev.* **1993**, *121*, 764–787. [CrossRef]

22. Jakob, C.; Siebesma, A.P. A new subcloud model for mass-flux convection scheme: Influence on triggering, updraft properties, and model climate. *Mon. Weather Rev.* **2003**, *131*, 2765–2778. [CrossRef]
23. Bechtold, P.; Kohler, M.; Jung, T.; Doblas-Reyes, F.; Leutbecher, M.; Rodwell, M.; Vitart, F.; Balsamo, G. Advances in simulating atmospheric variability with the ECMWF model: From synoptic to decadal time-scales. *Quart. J. R. Meteor. Soc.* **2008**, *134*, 1337–1351. [CrossRef]
24. Han, J.-Y.; Hong, S.-Y.; Kwon, Y.C. The performance of a revised simplified Arakawa-Schubert (SAS) convection scheme in the medium-range forecasts of the Korean Integrated Model (KIM). *Weather Forecast.* **2020**, *35*, 1113–1128. [CrossRef]
25. Arakawa, A.; Wu, C.-M. A Unified representation of deep moist convection in numerical modeling of the Atmosphere. Part I. *J. Atmos. Sci.* **2013**, *70*, 1977–1992. [CrossRef]
26. Grell, G.A.; Freitas, S.R. A scale and aerosol aware stochastic convective parameterization for weather and air quality modeling. *Atmos. Chem. Phys.* **2014**, *14*, 5233–5250. [CrossRef]
27. Chun, H.-Y.; Baik, J.-J. Weakly nonlinear response of a stably stratified atmosphere to diabatic forcing in a uniform flow. *J. Atmos. Sci.* **1994**, *51*, 3109–3121. [CrossRef]
28. Kim, Y.-J.; Arakawa, A. Improvement of orographic gravity wave parameterization using a mesoscale gravity wave model. *J. Atmos. Sci.* **1995**, *52*, 1875–1902. [CrossRef]
29. Kim, Y.-J.; Doyle, J.D. Extension of an orographic-drag parameterization scheme to incorporate orographic anisotropy and flow blocking. *Quart. J. R. Meteor. Soc.* **2005**, *131*, 1893–1921. [CrossRef]
30. Han, J.; Witek, M.L.; Teixeira, J.; Sun, R.; Pan, H.L.; Fletcher, J.K.; Bretherton, C.S. Implementation in the NCEP GFS of a hybrid eddy-diffusivity mass-flux (EDMF) boundary layer parameterization with dissipative heating and modified stable boundary layer mixing. *Weather Forecast.* **2016**, *31*, 341–352. [CrossRef]
31. Clough, S.A.; Shephard, M.W.; Mlawer, E.J.; Delamere, J.S.; Iacono, M.J.; Cady-Pereira, K.; Boukabara, S.; Brown, P.D. Atmospheric radiative transfer modeling: A summary of the AER codes. *J. Quant. Spectrosc. Radiat. Transf.* **2005**, *91*, 233–244. [CrossRef]
32. Pan, H.-L.; Liu, Q.; Han, J.; Sun, R. Extending the Simplified Arakawa-Schubert Scheme for Meso-Scale Model Applications. *NCEP Off. Note* **2014**, *10*, 479. Available online: http://www.lib.ncep.noaa.gov/ncepofficenotes/files/on479.pdf (accessed on 1 December 2021).
33. Hersbach, H.; Bell, B.; Berrisford, P.; Biavati, G.; Horányi, A.; Muñoz Sabater, J.; Nicolas, J.; Peubey, C.; Radu, R.; Rozum, I.; et al. ERA5 Hourly Data on Single Levels from 1979 to Present. Copernicus Climate Change Service (C3S) Climate Data Store (CDS). 2018. Available online: https://rda.ucar.edu/datasets/ds633.0 (accessed on 1 December 2021).
34. Huffman, G.J.; Bolvin, D.T.; Nelkin, E.J.; Adler, R.F. *TRMM (TMPA) Precipitation L3 1 Day 0.25 Degree × 0.25 Degree V7*; Andrey Savtchenko, A., Ed.; Goddard Earth Sciences Data and Information Services Center (GES DISC): Greenbelt, MD, USA, 2016.